Journal of Molecular Catalysis A: Chemical 352 (2012) 95–101

Contents lists available at SciVerse ScienceDirect

Journal of Molecular Catalysis A: Chemical

journal homepage: www.elsevier.com/locate/molcata

The photocatalytical activities for water decomposition of $K_4R_2M_{10}O_{30}$ (R = Y, La, Ce, Nd, Sm; M = Ta, Nb) and their photophysical properties based on the first principle calculation

Mengkui Tian [a,b], Wenfeng Shangguan [c,*], Wenliang Tao [a]

[a] School of Chemistry and Chemical Engineering, Guizhou University, Guiyang City, Guizhou Province 550003, PR China
[b] Department of Chemical System Engineering, School of Engineering, The University of Tokyo, Hongo 7-3-1, Bunkyo Ku, Tokyo 113-8656, Japan
[c] Research Center for Combustion and Environmental Technology, Shanghai Jiao Tong University, Shanghai 200240, PR China

ARTICLE INFO

Article history:
Received 27 August 2011
Received in revised form 24 October 2011
Accepted 26 October 2011
Available online 4 November 2011

Keywords:
Photocatalyst
$K_4R_2M_{10}O_{30}$ (R = Y
La
Ce
Nd
Sm
M = Ta
Nb)
Water decomposition
Electronic structure

ABSTRACT

Series of photocatalysts $K_4R_2M_{10}O_{30}$ (R = Y, La, Ce, Nd, Sm; M = Ta, Nb) were presented as iso-structural compounds by solid-state reaction method. These photocatalysts showed water decomposition activities under $\lambda > 300$ nm irradiation with Na_2SO_3 and $AgNO_3$ solution acting as hole and electron scavenges respectively. Among them, R = Ce demonstrated water decomposition activities under visible light irradiation ($\lambda > 420$ nm) and R = La showed overall water splitting activities under $\lambda > 300$ nm irradiation. The first principle calculation based on density functional theory with Plane-wave pseudo potential method and Generalized Gradient Approximation was conducted on M = Nb as representatives to investigate their electronic structure closely, so did on their precursor oxides. Combined with the electronic structures and absorption properties, the band structures of $K_4R_2M_{10}O_{30}$ (R = Y, La, Ce, Nd, Sm; M = Ta, Nb) were proposed and this model of band structure is in good agreement with their photocatalytical activities. Furthermore, the visible light responsive ability of R = Ce, as the only one among them, is regarded as the hybridization and overlap of partial occupied and unoccupied Ce 4f with O 2p and Nb 4d (Ta 5d), while in other cases, the band gap transition from O 2p to Nb 4d Ta (5d), which mainly consist their valence band and conduction band respectively, is dominant. Furthermore, there showed obvious inherent relationship between $K_4R_2M_{10}O_{30}$ (R = Y, La, Ce, Nd, Sm; M = Ta, Nb) and their precursor rare earth oxides in terms of electronic structure and photophysical properties.

1. Introduction

The development of hydrogen energy attracts more and more attention for it is a promise way to settle current confronted energy depletion and environmental problems [1–3]. Among these methods or reactions employed to develop hydrogen, this decomposing water into H_2 and O_2 photocatalytically under solar energy irradiation to transfer solar energy into H_2 as chemical energy carrier, called solar-hydrogen, is one of the most ideal ways considering resource sustainability, environmental and cost issues [4,5]. The urgent work for photocatalytical water decomposition is to design and develop semiconductor photocatalysts with appropriate band gap to make the best use of solar energy and band edges to meet oxidization and reduction water requirement as well as high quantum yield and high stability [6–8]. Up to now, many oxides possessing d^0 electronic configuration such as TiO_2, ZrO_2, ZnO, WO_3, a-Fe_2O_3, $SrTiO_3$, $K_4Nb_6O_{17}$, $NaTaO_3$, as well as oxides possessing d^{10} electronic configuration such as Zn_2GeO_4, $SrIn_2O_4$, $NaSbO_3$, etc., have been investigated [9–13]. Unfortunately, most of them failed to satisfy the above-mentioned requirements simultaneously. Band engineering methods such as doping with metal cations (Fe^{3+}, Cr^{3+}, Ni^{+}) and anions (N, C, S, P, B and halogen family) were extensively studied to extend their absorption edges. However, these doping levels formed in forbidden band are generally discrete and the mobility of electrons and holes in the doping levels is poor, consequently, resulting in low quantum efficiency, instability and limited visible light responsive defects [14–16].

Moreover, theoretical analysis for electronic structure based on the first principle calculation is recognized as an efficient way to bridge the relationship between inherent electronic structures and the apparent photo-physical and photocatalytical properties of a photocatalyst, in turn, providing theoretical basis to develop new visible light driven photocatalysts, for example, these oxy(nitrides) Ta_3N_5, TaON, $LaTiO_2N$, and oxy(sulfides) $LnTi_2S_2O_5$, $Sm_2Ti_2S_2O_5$ as well as these solid solution compounds, such as $(AgIn)_{(x)}Zn_{2(1-x)}S_2$, $Ga_{1-x}N_{1-x}Zn_xO_x$ [17–21].

* Corresponding author. Tel.: +86 21 34206020; fax: +86 21 34206020.
E-mail addresses: tianmk@hotmail.com (M. Tian), shangguan@sjtu.edu.cn (W. Shangguan).

1381-1169/$ – see front matter © 2011 Elsevier B.V. All rights reserved.
doi:10.1016/j.molcata.2011.10.019

Furthermore, since the similar properties of rare earth elements, in many cases, for a new rare earth photocatalyst, substituting the rare earth element by other rare earth element to form series of isostructural compounds and investigating their difference on photocatalytical and photophysical properties was conducted, such as $LnTaO_4$ (Ln = La, Ce, Pr, Nd, and Sm) [22], Bi_2RNbO_7 (R = Y, rare earth) [23], etc. As for the Ln 4f^r role and contribution to their band configuration, there were different conclusions for different compounds. Although those conclusions were different and even contradictory in some case, there was a common point that these proposes were based on the distribution and position of the energy states of Ln 4f relative to other energy level.

In our previous work [24], $K_4Ce_2M_{10}O_{30}$ (M = Ta, Nb) were presented as new photocatalysts for water decomposition under visible light irradiation. In this paper, some rare earth elements substituting of Ce in photocatalysts $K_4Ce_2M_{10}O_{30}$ (M = Ta, Nb), denoted as $K_4R_2M_{10}O_{30}$ (R = Y, La, Ce, Nd, Sm; M = Ta, Nb), were presented and their differences on photocatalytical and photophysical properties were analyzed based on the first principle calculation on their electronic structures.

2. Experimental

2.1. Preparation

$K_4R_2M_{10}O_{30}$ (R = Y, La, Ce, Nd, Sm; M = Ta, Nb) were synthesized by conventional high temperature solid-state reaction method. High purity of $K_2CO_3{\cdot}3H_2O$, Y_2O_3, La_2O_3, $Ce(NO_3)_3{\cdot}6H_2O(CeO_2)$, Nd_2O_3, Sm_2O_3, as well Ta_2O_5 (Nb_2O_5) with corresponding ratio were mixed finely, firstly calcinated at 800 °C for 5 h then 1100 °C for 12 h, with a regrinding process in between. Excess $K_2CO_3{\cdot}3H_2O$ (ca. 20%) was used to compensate for the loss caused by volatilization during calcination. The synthesized samples were identified by X-ray diffraction on Bruker-AXS D8 Advance with Cu Kα radiation (λ = 1.540562 Å). UV–vis diffusion reflectance spectra were recorded using TU-1901 spectrophotometer. The reflectivity spectrum was transformed to absorbance intensity through Kubelka–Munk method. The BET surface areas were determined from N_2 adsorption–desorption isotherm on Quantachrome NOVA 1000-TS. The SEM image was obtained on FEI SIRION 200.

2.2. Photocatalytical reaction

The photocatalytical reaction was carried out in a Pyrex reactor, which allows the transmission of photon with wavelength more than 300 nm, and visible light irradiation condition was controlled by a cut-off (λ > 420 nm) filter to remove UV light. 0.2 g as prepared photocatalyst in powder was dispersed into 100 ml aqueous solution of 0.2 M Na_2SO_3 or 0.1 M $AgNO_3$ in the reactor with stirring under irradiating by 300 W Xe lamp. Evolved H_2 and O_2 were measured by gas chromatography (QC-9101) with thermal conductivity detector (TCD) with high purity Ar as carrier gas.

2.3. The first principle calculation

The first principle calculation based on Density Functional Theory was conducted by CASETP package with Plane-wave pesudopotential method and Generalized Gradient Approximation [25]. The core orbitals were replaced by the ultrasoft core potentials, and the K $3s^23p^64s^1$, O $2s^24p^4$, Nb $4s^24p^64d^45s^1$, La $5s^25p^65d^16s^2$, Ce $4f^15s^25p^65d^16s^2$, Sm $4f^65s^25p^66s^2$, Nd $4f^45s^25p^66s^2$ and Y $4s^24p^64d^15s^2$ electrons were treated explicitly. The kinetic energy cutoff was set at 330 eV.

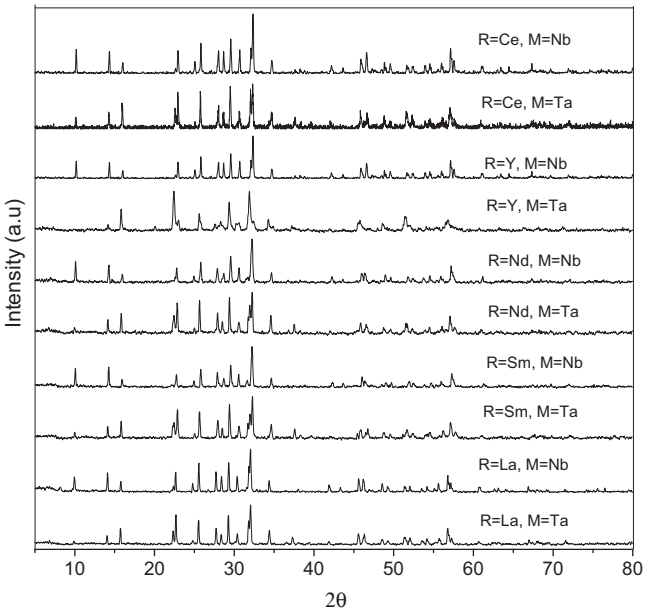

Fig. 1. The XRD patterns for $K_4R_2M_{10}O_{30}$ (R = Y, La, Ce, Nd, Sm; M = Ta, Nb).

3. Results and discussions

3.1. Characterizations

Usually, tantalates and niobates form iso-structural compounds for the similar properties of atom Ta and Nb, especially the diameter of their cations (0.68 Å for Ta^{5+} and 0.69 Å for Nb^{5+}) [26]. There is no exception on $K_4Ce_2M_{10}O_{30}$ (M = Ta, Nb), being with the same tetragonal tungsten bronze structure [27], and these series of $K_4R_2M_{10}O_{30}$ (R = Y, La, Ce, Nd, Sm; M = Ta, Nb) also showed iso-structural, as identified from XRD patterns in Fig. 1. The UV–vis diffusion reflectance spectra of these iso-structural compounds were shown in Fig. 2. It revealed that only these R = Ce showed visible light responsive ability, for M = Ta and Nb, corresponding to absorption edges of 540 nm and 710 nm respectively. More interesting case is that the absorption edges for these M = Nb showed obvious red-shift of about 70 nm compared with those for M = Ta, which can be regarded as the lower energy level of Nb

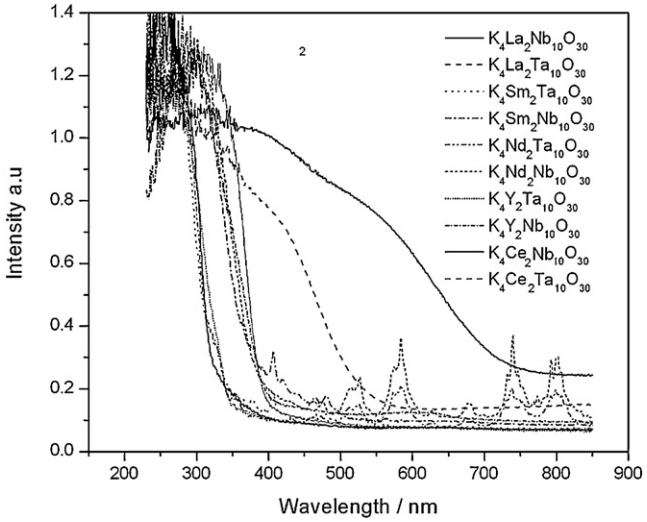

Fig. 2. UV–vis diffusion reflectance spectra of $K_4R_2M_{10}O_{30}$ (R = Y, La, Ce, Nd, Sm; M = Ta, Nb).

4d than that of Ta 5d and consequently the narrower band gap according to results from previous studies [24,26]. Furthermore, for these samples of R = Sm, and Nd, besides the sharp absorption edges from their band gap transition, there also displayed some absorption peaks in visible light region, which is due to the internal energy gap transition and will be discussed in detail based on the results from the theoretical calculation in later section.

3.2. Photocatalytical activities

Their water decomposition activities under different conditions were shown in Table 1. It can be seen that all of them showed photocatalytical water decomposition activities to evolve H_2 and O_2 under $\lambda > 300$ nm irradiation with Na_2SO_3 and $AgNO_3$ solution acting as hole and electron scavenger respectively. Meanwhile, for a given rare earth compounds, these M = Ta showed higher activities for H_2 evolution than that of M = Nb. Since only R = Ce demonstrated visible light responsive ability, so there carried out measurement under $\lambda > 420$ nm irradiation for R = Ce. Actually they exhibited good half reaction to evolve H_2 and O_2, as shown in Table 1 elsewhere. When it comes to pure water without any sacrificial regent and under $\lambda > 300$ nm irradiation, only this R = La showed overall water splitting activities. And the less evolved O_2 compared with its theoretical value maybe ascribes to some degree of dissolution of O_2 in water and physical or chemical absorption of O_2 on the surface of photocatalyst. Additionally, O_2 is less sensitive to Ar carrier in TCD detector than that of H_2, so it was difficult to detect small amount of evolved O_2. In general, the photocatalytical activity is proportional to the surface area and efficient photons absorbed of a photocatalyst. The more surface area, the more active reaction sites involved and the more efficient photons absorbed, the more electron–hole pairs generated. In this paper, taking $K_4Ce_2M_{10}O_{30}$ (M = Ta, Nb) as an example, also as discussed in Ref. [24], although the surface area for M = Nb is about 2.65 m^2/g and 1.67 m^2/g for M = Ta, the activities for H_2 evolution for M = Ta is greater than that from M = Nb even though the efficient incident photons absorbed by M = Nb is more than that from M = Ta for their difference of absorption properties (absorption edges for M = Ta is 540 nm, and 710 nm for M = Nb). Similar phenomenon happened on other photocatalysts as shown in Table 1. Since these iso-structure compounds were prepared by the same method and condition, their differences in terms of crystallite, morphology, and surface properties are not so significant, as shown from their SEM images (take M = Nb as examples) in Fig. 3 and their BET surface area in Table 1. Consequently, it is proposed that their differences in photocatalytical activities mainly result from their inherent electronic structures, which will be discussed closely in later section.

3.3. Electronic structures for $K_4R_2M_{10}O_{30}$ (R = Y, La, Ce, Nd, Sm; M = Ta, Nb)

Since the electronic structure of a photocatalyst is a dominate factor affecting its photophysical and photochemical properties, the study of it is well recognized as an efficient way to connect its inherent structure and its apparent photophysical and photocatalytical properties [28,29]. As for the study of electronic structure of a semiconductor photocatalyst, the first principle calculation based on density functional theory is a powerful tool. The calculated results include theoretical band gap (Total and Partial or Projected), density of states, and energy contour for electron in certain region, etc. Based on the calculated band structure, it can be proposed the band configuration, especially the top of valence band and the bottom of conduction band of a photocatalyst, which is important to determine it's potential ability to reduce and oxidize water or not, and is also the basis for band engineering method to tailor and develop new semiconductor materials.

Since the similar electronic structures and properties of these iso-structural tantalates and niobates except for their conduction band mainly result from Ta 5d and Nb 4d respectively in most cases, so here make these M = Nb as examples to investigate their band structures and absorption properties closely and assume that analogous results apply on M = Ta correspondingly.

For these band structures of $K_4R_2M_{10}O_{30}$ (R = Y, La, Ce, Nd, Sm; M = Ta, Nb), they can be classfied into three types. One is these without occupied R 4f, including R = La, and Y. In this type, take R = La as an example and its density of states is shown in Fig. 4(a). The theoritical band gap for Ln = La was about 2.1 eV, less than that of 3.18 eV from experimental data, which is frequently pointed out as a common feature of DFT calculations for the discontinuity in the exchange-correlation potential is not taken into account within the framework of density functional theory. The configuration of its band structures illustrated in Fig. 4(a) is as following: the top of the valence band mainly consists of O 2p, while the bottom of conduction band is from Nb 4d. Since the empty of La 4f, it was not taken into consideration as valence electron here. The absorption edge at 390 nm for $K_4R_2Nb_{10}O_{30}$ (R = La) is mainly due to the band gap transition from O 2p to Nb 4d, so do this for $K_4R_2Ta_{10}O_{30}$ (R = La), from O 2p to Ta 5d. The similar analysis is suitable for R = Y since it is also empty of Y 4f.

The second type is these with partial occupied R 4f but demonstrating no visible light responsive properties, including R = Nd and Sm. Here take R = Sm shown in Fig. 4(b), as an example to investigate closely. The theoretical band gap for R = Sm in $K_4R_2Nb_{10}O_{30}$ is about 1.4 eV, while its experimental band gap is about 3.3 eV. The configuration for the top of valence band is mainly due to O 2p, while the bottom of conduction band is attributed to Nb 4d. It is worthy to noting that there is a high density states of Sm 4f between the band gap, and it is high localized rather than hybridization or overlap with other energy level. Here how to ascribe the role of this high localized Sm 4f to the band structure and the effect on the photophysical and photocatalytical properties is very important and interesting. From the DRS of $K_4Sm_2Nb_{10}O_{30}$ in Fig. 2, it is obvious to show sharp band transition at 375 nm, and accompanying with some discrete energy transition at visible light region, such as at 430 nm, 520 nm, etc. For the sharp band gap transition at 375 nm, it can be ascribed to the direct transition from O 2p to Nb 4d, which mainly consist the valence band and conduction band respectively, as mentioned previously. When it comes to the energy gap transition properties, it is proposed as the transition among these O 2p → Sm 4f or Sm 4f → Nb 4d and these energy states among splitted Sm 4f. Here also proposed that analogous case occurs on the R = Nd for it shows similar electronic structure and absorption properties as that of R = Sm.

The third and also the most interesting type is these R = Ce, for it is the only one showing visible light responsive ability in these series compounds. From the electronic structure presented in Fig. 4(c), it can be proposed that the band structure for $K_4Ce_2Nb_{10}O_{30}$ as following: the top of the valence band is consisted of O 2p, Nb 4d and some part contribution from this occupied Ce 4f, while the bottom of the conduction band is mainly ascribed to the unoccupied Ce 4f and Nb 4d. In this case, the Ce 4f is splitted into partial occupied Ce 4f and unoccupied Ce 4f, and it is the hybridization among the occupied of Ce 4f with O 2p and unoccupied Ce 4f with Nb 4d that increase the top of the valence band and at the same time expand the width of conduction band [22]. As a consequence, these R = Ce show visible light driven properties. In addition, among all of them, the K 3s and 3p always display high localized properties, which are regarded as little contribution to their band structure, while just contributing to their crystal structure and valence balance [5].

Table 1
Photocatalytical water decomposition activities on $K_4R_2M_{10}O_{30}$ (R = Y, La, Ce, Nd, Sm; M = Ta, Nb).

R = Y, La, Ce, Nd, Sm; M = Ta, Nb		BET surface area (m^2/g)	Absorption edge (nm)	Band gap (eV)	Activitities[a]/μmol		Activitities[b]/μmol		Activitities[c]/μmol	
					H_2	O_2	H_2	O_2	H_2	O_2
R = Y	M = Ta	2.05	350	3.54	3.5	6.2	–	–	0.0	0.0
	M = Nb	2.23	415	2.99	2.1	7.5	–	–	0.0	0.0
R = La	M = Ta	1.87	315	3.94	23.8	34.1	–	–	18.2	7.3
	M = Nb	1.71	390	3.18	14.3	30.4	–	–	6.2	1.8
R = Ce	M = Ta	1.67	540	2.29	28.6	22.7	14.5	9.8	3.1	0.0
	M = Nb	2.65	710	1.75	18.4	21.8	5.6	8.6	0.7	0.0
R = Nd	M = Ta	2.51	330	3.76	2.3	5.9	–	–	0.0	0.0
	M = Nb	2.37	405	3.06	1.8	4.0	–	–	0.0.	0.0
R = Sm	M = Ta	1.34	325	3.82	6.8	13.2	–	–	0.0	0.0
	M = Nb	1.58	375	3.31	3.3	7.2	–	–	0.0	0.0

0.2 g photocatalyst in powder dispersing into 100 ml solution in Pyrex reactor, irradiating by 300 W Xe lamp for 4 h.
[a] 0.2 M Na_2SO_3 and 0.1 M $AgNO_3$ solution acting as hole and electron scavenger respectively without filter.
[b] With λ > 420 nm filter (only carried out on R = Ce).
[c] In pure water without filter.

3.4. The electronic structures for precursor oxides

In order to investigate the electronic structure of $K_4R_2Nb_{10}O_{30}$ closely, especially the difference among them, the electronic structures of precursor oxides La_2O_3, Sm_2O_3 and CeO_2, corresponding to the three types mentioned above, are shown in Fig. 5. For La_2O_3, as shown in Fig. 5(a), it is obvious that the direct band excitation from O 2p → La 5d is dominant and the band structure is resulting from the covolent bonding properties of O 2p and La 5d, which is consistant with $K_4La_2Nb_{10}O_{30}$. As for Sm_2O_3, as shown in Fig. 5(b), the most obvious character is the high localized density states of Sm 4f and some splitted energy states near to it, among which is ascribed to the energy gap transition in visible light region on DRS spectrum. Although the band gap transition from O 2p to Sm 4f in Sm_2O_3 is obvious, as for $K_4Sm_2Nb_{10}O_{30}$, the band gap transition from O 2p to Nb 4d is dominant for the high localized properties of

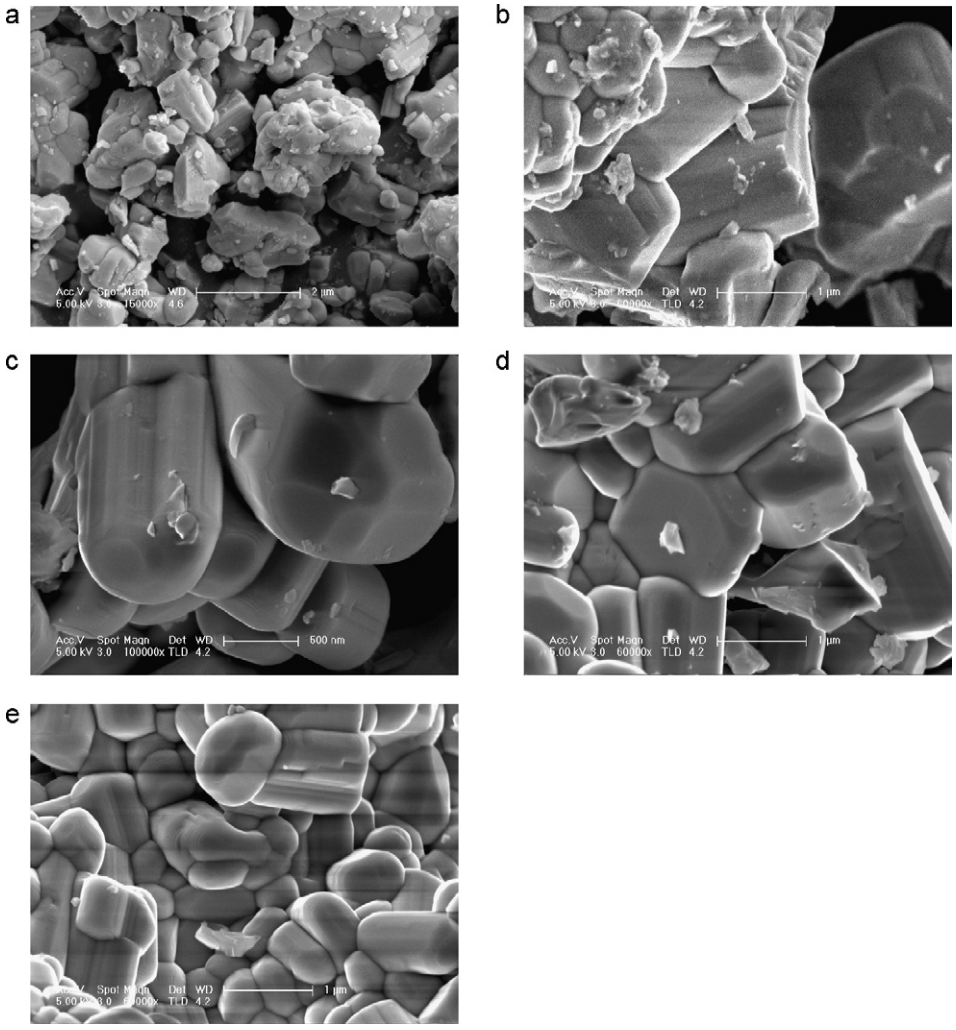

Fig. 3. SEM images for $K_4R_2Nb_{10}O_{30}$, (a) for R = Y, (b) for R = La, (c) for R = Ce, (d) for R = Nd and (e) for R = Sm.

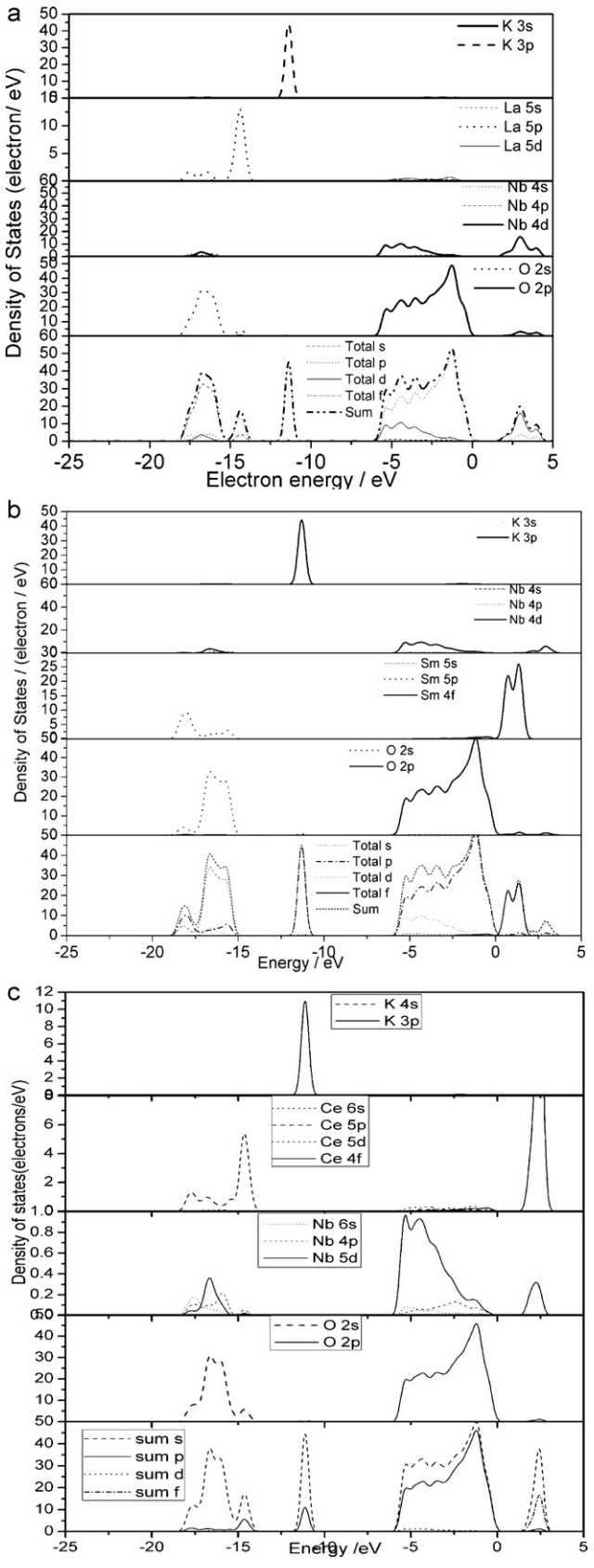

Fig. 4. Partial density of states for $K_4R_2Nb_{10}O_{30}$, where (a), (b), (c) corresponding to R = La, Sm and Ce repectively.

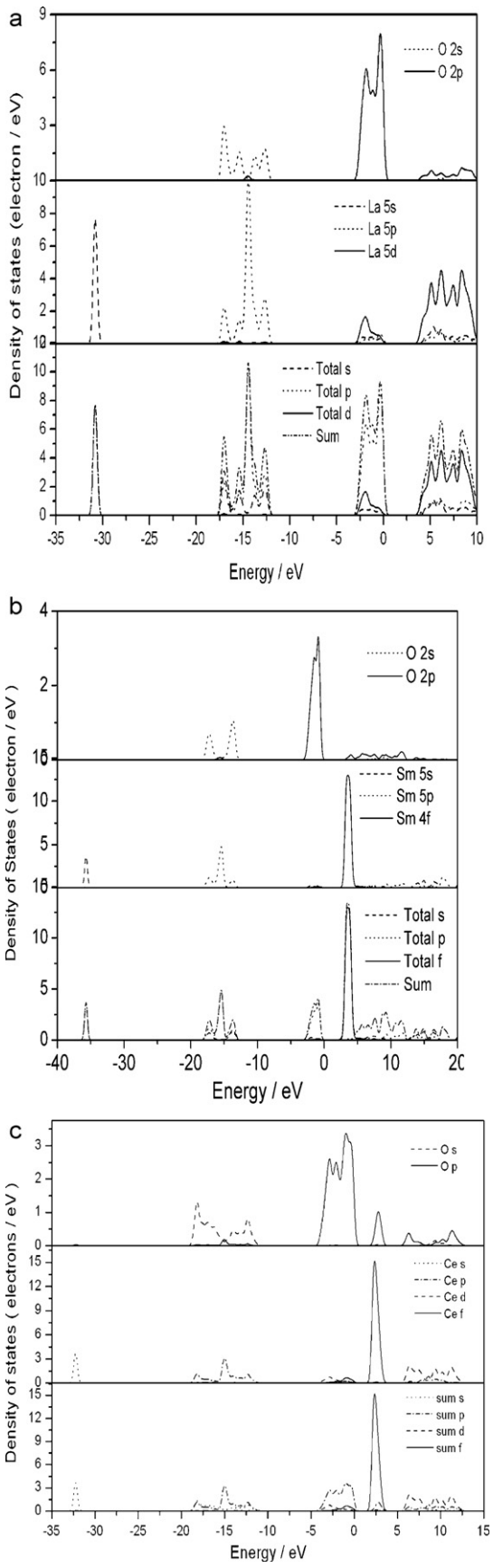

Fig. 5. Partial density of states for (a) La_2O_3, (b) Sm_2O_3 and (c) CeO_2.

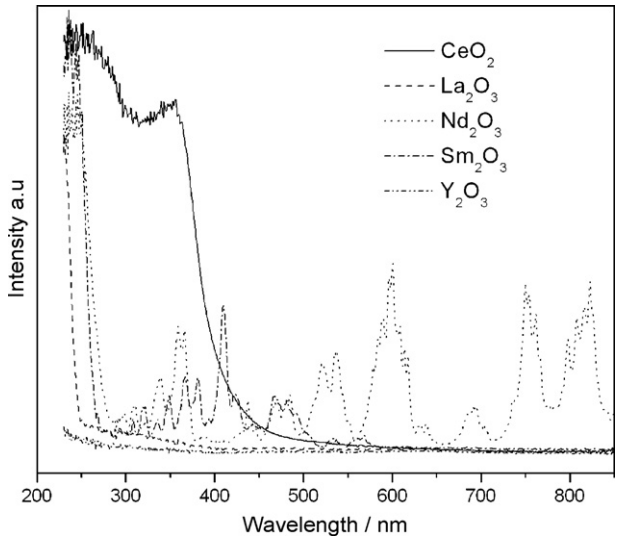

Fig. 6. UV–vis diffuse reflectance spectra for precursor rare earth oxides.

Sm 4f. When it comes to CeO_2, it is worthy to noting that the Ce 4f is splitted into partial occupied and unoccupied parts hybridizing with O 2p, which is agree with that from $K_4Ce_2Nb_{10}O_{30}$.

The UV–visible DRS spectra of these oxides precursors were measured and illustrated in Fig. 6. It can be seen that the absorption edge of CeO_2 is red-shift obviously compared with other oxides, which is consistent with its electronic structure. Although CeO_2 shows some degree of visible light responsive properties (absorption edge is about 430 nm), the visible light driven properties of $K_4Ce_2M_{10}O_{30}$ (M = Ta, Nb) are not regarded as resulting from it for there is no CeO_2 phase in as prepared $K_4Ce_2M_{10}O_{30}$ (M = Ta, Nb) and their absorption edges are more red-shift than that of CeO_2. For La_2O_3 and Y_2O_3, their sharp absorption edges are at 250 nm and 180 nm respectively, indicating the band gap transition properties obviously. While for Sm_2O_3 and Nd_2O_3, there are many absorption peaks in visible light region resulting from internal transition in a partly filled 4f shell except for the sharp band gap transition in 270 nm and 285 nm respectively. Not only the shape but also the position of these peaks in simple sesquioxide (R_2O_3) are consistent with those in $K_4R_2M_{10}O_{30}$ (R = Nd, Sm; M = Ta, Nb). Moreover, all of these variation of band structure and absorption properties agreed with that in simple sesquioxides of R closely associated with the energy levels of R 4f in the electronic structure of these $K_4R_2M_{10}O_{30}$ (R = Y, La, Ce, Nd, Sm; M = Ta, Nb).

3.5. Band structure model

Combined with their electronic structures and absorption properties, the band structure model for $K_4R_2Nb_{10}O_{30}$ (R = Y, La, Ce, Nd, Sm) can be proposed schematically as shown in Fig. 7. Since O 2p is dominant for valence band in many cases, which is located at 3.0 V vs. NHE, and the Nb 4d is located at −0.7 V vs. NHE in $Sr_2M_2O_7$ [26], so it is reasonable to determine the band edges positions of $K_4R_2Nb_{10}O_{30}$ (R = Y, La, Ce, Nd, Sm). As illustrated in Fig. 7, for these without occupied R 4f, such as R = Y and La, their band gap transition is from O 2p to Nb 4d. For the visible light driven R = Ce, it is also suggested that unoccupied as well as occupied Ce 4f orbitals are not completely localized but hybridized with O 2p and Nb 4d orbital, which is contributing for the decrease of the band gap. As for R = Nd and Sm, there show high localized properties of Nd 4f and Sm 4f between band gap. These localized characters of R 4f are consistent with that of $RbLnTa_2O_7$ (Ln = La, Pr, Nd, and Sm) [30] and $R_3Nb(Ta)O_7$ (R = Y, Yb, Gd, La) [31]. Moreover, the suggested band structure is in good agreement with their photocatalytical activities for water decomposition shown in Table 1 elsewhere. There showed the highest and overall water splitting activities on R = La for its pure and perfect band structure. Although R = Y is similar with R = La in terms of band structure, it showed lower activities for crystal distortion resulting from its smaller ion radius, which is recognized as a negative factor affecting the transfer of photo-generated charge carriers. As for these R = Nd and Sm, they showed lower activities compared with that of R = La. The reason may be due to the high localized properties of Sm 4f and Nd 4f between band gaps, which act as recombination centers for charge carriers. When it comes to R = Ce, it demonstrated activities between that of R = La and R = Sm or R = Nd. Since its absorption edge shifts to about 710 nm, it should show great promotion activities for it absorb more efficient incident photons than that of R = La, but unfortunately, it showed medium activities, which can be ascribed to the poor transfer ability of photo-generated charges on the conduction band of

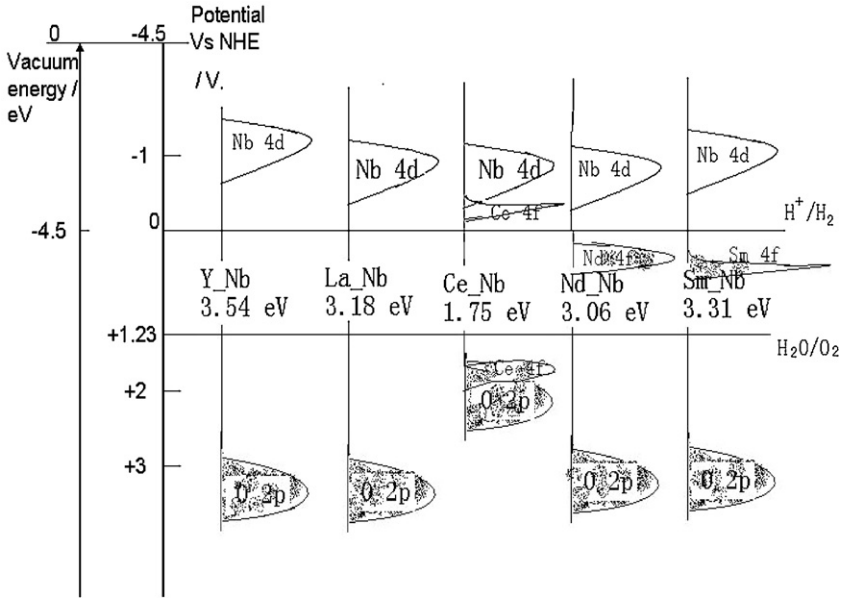

Fig. 7. Proposed schematic band structure for $K_4R_2Nb_{10}O_{30}$ (R = Y, La, Ce, Nd, Sm).

R = Ce. Although Ce 4f is not high localized between band gap, the hybridization or overlap with Nb 4d and O2p in some degree is also poor to facilitate the transfer of charge carriers. Therefore, the photocatalytical activity seems to be closely related to the degree of the R–O–Nb hybridization, which affects not only the edges of conduction band and valence band but also the transfer ability of photo-generated charges. In addition, the higher activities for hydrogen evolution on these M = Ta in any case is regarded as the result of higher energy of Ta 5d than that of Nb 4d, mainly contributing to their conduction band correspondingly. It is well known that the higher the energy level of band edge, the higher driven force to evolve hydrogen photocatalytically. As for O_2 evolution, they showed little difference for the same R on M = Ta and Nb for their valence band are mainly from O 2p, but for different R, the difference of O_2 evolution is obvious as a result of difference for their electronic structure as analyzed previously.

4. Conclusions

In conclusions, series of rare earth compounds $K_4R_2M_{10}O_{30}$(R = Y, La, Ce, Nd, Sm; M = Ta, Nb) were presented as iso-structural compounds and showed water decomposition activities. Based on the results from the first principle calculation and combined with their absorption properties, the band structure of these series of $K_4R_2M_{10}O_{30}$ (R = Y, La, Ce, Nd, Sm; M = Ta, Nb) were proposed. Among them, only R = Ce demonstrated visible light responsive properties as a result of the inter-hybridization of Ce 4f, O 2p and Nb 4d (Ta 5d). For these without filled R 4f, such as R = La and Y, the direct band gap transition from O 2p to Nb 4d (Ta 5d) is dominant. And for these with partial filled Ln 4f, such as R = Sm, Nd, besides the dominant band gap transition from O 2p to Nb 4d (Ta 5d), there accompany with other energy gap transition resulting from discrete energy states. Especially, the electronic structure and absorption properties of these series of photocatalysts have obvious inherent relationship with their precursor rare earth oxides, which were also investigated closely on their electronic structure and UV–vis diffusion reflectance spectra. Furthermore, their proposed band structure is in good agreement with their photocatalytical activities for water decomposition.

Acknowledgments

This work was supported financially by the National Basic Research Program of China (973 Program, 2009CB220004), the National Natural Science Foundation (21103028) and Key Program of Society Development (SZ [2008]3008), Guizhou Province; Key Program of Science and Technology ([2008] 014), Guiyang City.

References

[1] S.N. Lewis, Science 315 (2001) 798–801.
[2] N.Z. Muradov, T.N. Vezirolu, Int. J. Hydrogen Energy 30 (3) (2005) 225–237.
[3] M. Grätzel, Nature 414 (2001) 338–344.
[4] A. Fujishima, K. Honda, Nature 238 (1972) 37–38.
[5] A. Kudo, Y. Miseki, Chem. Soc. Rev. 38 (2009) 253–278.
[6] A. Kudo, Int. J. Hydrogen Energy 31 (2) (2006) 197–202.
[7] R.V. Krol, Y.Q. Liang, J. Schoonman, J. Mater. Chem. 18 (2008) 2311–2320.
[8] B.D. Alexander, P.J. Kulesza, I. RutKowska, R. Solarska, J. Auguskynski, J. Mater. Chem. 18 (2008) 2203–2298.
[9] M. Ni, M.K.H. Leung, D.Y.C. Leung, K. Sumathy, Renew. Sustain. Energy Rev. 11 (2007) 401–405.
[10] G. Liu, L. Wang, H. Yang, H. Cheng, G. Lu, J. Mater. Chem. 20 (2010) 831–843.
[11] X.B. Chen, S.S. Mao, Chem. Rev. 107 (2007) 2891–2959.
[12] A. Kay, I. Cesar, M. Grätzel, J. Am. Chem. Soc. 128 (2006) 15714–15721.
[13] J. Sato, N. Saito, H. Nishiyama, Y. Inoue, J. Phys. Chem. B 105 (26) (2001) 6061–6063.
[14] H. Kato, A. Kudo, J. Phys. Chem. B 106 (19) (2002) 5029–5034.
[15] A. Kudo, M. Sekizawa, Chem. Commun. 15 (2000) 1371–1372.
[16] R. Asahi, T. Morikawa, T. Ohwaki, K. Aoki, Y. Taga, Science 293 (2001) 269–271.
[17] M. Hara, G. Hitoki, T. Takata, J.N. Kondo, H. Kobayashi, K. Domen, Catal. Today 78 (1–4) (2003) 555–560.
[18] A. Kasahara, K. Nukumizu, T. Takata, J.N. Kondo, M. Hara, H. Kobayashi, K. Domen, J. Phys. Chem. B 107 (3) (2003) 791–797.
[19] A. Ishikawa, T. Takata, J.N. Kondo, M. Hara, H. Kobayashi, K. Domen, J. Am. Chem. Soc. 124 (45) (2002) 13547–13553.
[20] I. Tsuji, H. Kato, H. Kobayashi, A. Kudo, J. Am. Chem. Soc. 126 (41) (2004) 13406–13413.
[21] K. Maeda, K. Teramura, D. Lu, T. Takata, N. Saito, Y. Inoue, K. Domen, Nature 440 (2006) 295.
[22] M. Machida, S. Murakami, T. Kijima, J. Phys. Chem. B 105 (16) (2001) 3289–3294.
[23] Z.G. Zou, J.H. Ye, H. Arakawa, J. Phys. Chem. B 106 (3) (2002) 517–520.
[24] M.K. Tian, W.F. Shanguan, J. Yuan, L. Jiang, M. Chen, J. Shi, Z.Y. Ouyang, S.J. Wang, Appl. Catal. A: Gen. 309 (2006) 76–84.
[25] M.D. Segall, P.J.D. Lindan, M.J. Probert, C.J. Pickard, P.J. Hasnip, S.J. Clark, M.C. Payne, J. Phys.-Condens. Mat. 14 (11) (2002) 2717–2744.
[26] A. Kudo, H. Kato, S. Nakagawa, J. Phys. Chem. B104 (3) (2000) 571–575.
[27] F. Brik, R. Enjalbert, C. Roucau, J. Galy, J. Solid State Chem. 122 (1996) 7–14.
[28] J. Hafner, Acta Mater. 48 (1) (2000) 71–92.
[29] G. Liu, P. Niu, C. Sun, S.C. Smith, Z. Chen, G.Q. Lu, H. Cheng, J. Am. Chem. Soc. 132 (2010) 11642–11648.
[30] M. Machida, J. Yabunaka, T. Kijima, Chem. Mater. 2 (3) (2000) 812–817.
[31] R. Abe, M. Higashi, H. Arakawa, J. Phys. Chem. B 108 (2004) 811–814.